SCIENCE CHINA Materials ARTICLES

mater.scichina.com link.springer.com

Sci China Mater 2025, 68(10): 3675–3684
https://doi.org/10.1007/s40843-025-3516-2

The interface interaction of sulfur-doped carbon boosting kinetics of $Na_4Fe_3(PO_4)_2(P_2O_7)$ for high rate and stable sodium-ion batteries

Yuyang Cai[1,2†], Hanwen Cheng[2†], Zhuo Chen[2†], Hantao Xu[2†], Shidong Li[1,2], Jinghao Li[2], Yibo Zhang[1,2], Li Zhao[2], Zhenzhen Dou[2*] and Lin Xu[1,2,3,4*]

ABSTRACT Iron-based mixed phosphates are considered as promising cathode materials for sodium-ion batteries (SIBs) due to their low cost, non-toxicity, and high structural stability. However, their electrochemical performance is limited by poor electronic conductivity and sluggish ion diffusion. In this study, $Na_4Fe_3(PO_4)_2(P_2O_7)$ with porous coral-like S-doped carbon (NFPP-U0.5%) is presented as cathode materials for SIBs. The porous coral-like structure of the S-doped carbon layer, along with the C–S–Fe interaction, significantly enhances both electronic conductivity and sodium ion diffusion. NFPP-U0.5% delivers excellent rate performance, achieving a capacity of 80.3 mAh g^{-1} at 20 C. Moreover, the *in-situ* X-ray diffraction analysis reveals that the C–S–Fe interaction, combined with the unique carbon structure, contributes to a small lattice volume change during cycling. NFPP-U0.5% finally reached an ultra-long cycling life (capacity retention of 82.66% after 25,000 cycles at 20 C). The outstanding electrochemical performances and the unique interface interaction demonstrate that the S-doped carbon coating NFPP is of high potential as a cathode material for low cost and long-lasting cyclability energy storage system.

Keywords: sodium-ion batteries, mixed pyrophosphate, carbon coating, rate performance

INTRODUCTION

For many years, people have been exploring and improving technologies to utilize renewable energy sources such as wind, solar, and tidal energy. Among these efforts, the development of large-scale electric energy storage technologies (EESs), which can convert the renewable energy sources that are highly regionalized and cannot continuously and stably output into electrical energy, is very essential [1–9]. Sodium-ion batteries (SIBs) are considered as one of the most suitable choices for large-scale EESs due to abundant and widely distributed sodium resources, lower costs, and longer cycle lives. However, achieving high-performance SIBs is still a great challenge, especially to obtain high-performance and low-cost cathode materials for SIBs.

There are many kinds of cathode materials have been reported for SIBs, such as prussian blue analogs [9–15], transition-metal oxides [16–20], and polyanion compounds [21–30]. Considering the successful application of $LiFePO_4$ in lithium ion batteries and the mature production technology [31], many researchers have paid attention to the polyanion or mixed-polyanion compounds, which have three-dimensional (3D) framework that can provide strong structural support for the migration of Na^+ ions. Among various polyanion compounds, $Na_4Fe_3(PO_4)_2(P_2O_7)$ (NFPP) exhibits a high operating potential (~3.1 V vs. Na^+/Na) and high theoretical capacity (129 mAh g^{-1}) [32–34]. NFPP is a typical NASICON-type (sodium superionic conductor) structure material, which has a 3D crystalline framework that enables fast Na^+ transmission. Besides, it also has the advantages of low cost, high abundance, non-toxicity, and high structural stability. Although NFPP shows great potential, its practical electrochemical performance is still unsatisfied due to its low electronic conductivity and sluggish Na^+ diffusion kinetics, which lead to unstable cycle performance and unsatisfactory rate capabilities [32–36]. Therefore, it is crucial to find a low-cost and effective way to obtain a high rate and stable NFPP.

In order to reach the target of getting a high rate and stable NFPP, researchers have made various efforts. One of the most common modification methods is doping with other metal ions, usually transition metals or some inactive metal ions, such as Mg [37–39]. However, compared to Fe, the addition of other metals will increase the manufacturing costs, which will somehow increase the difficulty of the practical application of SIBs in the commercial EES market [34–37]. Another modification method is carbon coating, carbon coating can modify the electronic transport and enhance the electrochemical performance [40–44]. Currently, the carbon coating modification of NFPP mainly includes two categories: one focuses on using 3D structured graphene to support NFPP. Graphene-coated NFPP can achieve a significant performance improvement. However, graphene is expensive, and the synthesis process requires the addition of organic solvents, which does not align with the industrialization goals of sodium-ion battery cathodes. The other modification

---

[1] Hubei Longzhong Laboratory, Wuhan University of Technology (Xiangyang Demonstration Zone), Xiangyang 441000, China
[2] State Key Laboratory of Advanced Technology for Materials Synthesis and Processing, School of Materials Science and Engineering, Wuhan University of Technology, Wuhan 430070, China
[3] Hainan Institute, Wuhan University of Technology, Sanya 572000, China
[4] Zhongyu Feima New Material Technology Innovation Center (Zhengzhou) Co., Ltd., Zhengzhou 450001, China
[†] Equally contributed to this work.
[*] Corresponding author (email: dzz0881@whut.edu.cn; linxu@whut.edu.cn)

approach involves element doping of the carbon coating layer, but the mechanism of element doping of the carbon coating layer remains incomplete. Herein, we propose a simple and efficient S-doped carbon coating strategy that can greatly improve the rate performance and stability of NFPP and propose a new perspective on how S-doped carbon coating can influence the NFPP.

Aiming to improve the charge transfer and Na^+ kinetics and modify the morphology regulation of NFPP, we prepared NFPP with S-containing raw materials ($FeSO_4$) in which the S will transfer from the raw materials into the carbon coating layer and the content of S could be controlled with urea [45]. The S-contained samples are marked here as NFPP-S and NFPP-U0.5%. NFPP-S and NFPP-U0.5% have a coral-like structure and contain rich 3D pores, which are beneficial to increase the contact area between NFPP and electrolyte. We also studied the interaction between S-doped carbon coating and NFPP. The S element that was doped into the carbon layer will interact with the Fe^{2+} in NFPP to form C–S–Fe. The formation of C–S–Fe will help to improve the electron conductance and sodium ion diffusion property of NFPP. Besides, the C–S–Fe can also stabilize the lattice structure of NFPP during the cycle. Compared with the undoped NFPP/C composite material (NFPP), NFPP-U0.5% which regulates the S content by adding 0.5 wt% urea, shows highly enhanced rate performance (capacity of 80.3 mAh g^{-1} at 20 C) and ultra-long cycle life (15,000 cycles at 20 C, capacity retention rate of 92.63%). We proved the existence of C–S–Fe interaction through X-ray photoelectron spectroscopy (XPS), and revealed the impact of C–S–Fe interaction on the sodium ion diffusion through electrochemical kinetics analysis and material calculation. In addition, we also studied the lattice volume change of NFPP-U0.5% during charging and discharging through *in-situ* X-ray diffraction (XRD) analysis. This reasonable strategy makes NFPP a cost-effective, environmentally friendly, and highly stable cathode material for energy storage systems, which may promote the practical application of SIBs in the commercial EESs market in the near future.

RESULTS AND DISCUSSION

Morphology and structure characterizations

We successfully prepared the S-doped carbon coating NFPP using a facile one-step sol-gel method. The S source for the S-doped carbon coating comes from the sulfate in the raw material ($FeSO_4$). Since the ratio of raw materials is fixed in the synthesis process, we need to explore other methods to adjust the content of S in the carbon layer. Previous studies have shown that S in carbon materials is unstable and can easily combine with oxygen to produce SO_x by-products [46,47], which will greatly reduce the stability of the carbon material. However, the addition of N element will reasonably inhibit the combination of S element and O, thus may increase the content of S in the carbon layer. To achieve this, we introduced urea ($CO(NH_2)_2$) with a mass fraction of 0.5% to increase the N content in the carbon layer, thereby raising the S content. To confirm that N doping could increase the S in the carbon layer, we conducted CHONS testing to analyze the contents of N and S. As the results showed in Table S2, after adding 0.5% mass fraction of urea, the S element content was significantly increased by 0.456% along with the increase of N element by 0.07%. At the same time, to avoid the influence of the N element in $NH_4H_2PO_4$ on the experimental results of the increase of S content influenced by the urea addition, we synthesized the NFPP-NON (NFPP synthesized without N-containing raw materials) and NFPP-NON-U0.5% (NFPP synthesized without N-containing raw materials but added 0.5 wt% urea) to experimentally verify the effect of urea on increasing S content. The results in Table S2 showed that there is indeed a positive correlation between the content of N and S.

Here, we successfully prepared the S-doped carbon coating NFPP with the 0.5 wt% urea relative to the mass of citric acid and marked it as NFPP-U0.5%. We also prepared S-doped NFPP/C without using urea which is marked as NFPP-S, and NFPP/C which does not contain S but adds the same amount of urea and is marked as NFPP. To evaluate the phase constitution and lattice structure changes, XRD data were collected and refined for all samples. The Rietveld-refined results of NFPP-U0.5% with satisfactory weighted profile R-factors (R_{wp} = 2.714 %) are shown in Fig. 1a and Fig. S1, refined lattice parameters (a = 17.83976 Å, b = 6.49747 Å, c = 10.74048 Å, and V = 1244.963 $Å^3$) while the other two samples' refined lattice parameters are NFPP-S (a = 17.83445 Å, b = 6.46308 Å, c = 10.76465 Å, and V = 1240.794 $Å^3$) and NFPP (a = 17.78447 Å, b = 6.45956 Å, c = 10.77852 Å, and V = 1238.234 $Å^3$). The Rietveld refinement results are tabulated in Table S1. The refined lattice parameters and the left shift of XRD peaks (Fig. 1b) indicate that the lattice volume of NFPP, NFPP-S, and NFPP-U0.5% gradually increases. The unmatched diffraction peaks in the XRD pattern are attributed to the formation of the $NaFePO_4$ impurity phase during the synthesis process. As shown in Fig. 1c, NFPP belongs to the orthorhombic *Pn21a* space group. It has a typical NASICON-type framework structure with open 3D robust frameworks [32–45]. The open 3D robust frameworks provide sufficiently large vacant spaces for sodium ions diffusion. Theoretically, the increase in lattice volume will also lead to a larger channel inside NFPP, which is more conducive to the diffusion of sodium ions. Scanning electron microscopy (SEM) and transmission electron microscopy (TEM) technologies were employed to investigate the morphology of NFPP, NFPP-S, and NFPP-U0.5%. Fig. 1d shows the SEM image of NFPP, where no obvious pores are observed. In contrast, the SEM images of NFPP-S (Fig. 1e) and NFPP-U0.5% (Fig. 1f) clearly reveal a porous, coral-like structure. Fig. 1g illustrates the carbon coating layer with a thickness of 7 nm on the surface of NFPP-U0.5% nanoparticles, which is produced by the pyrolysis of citric acid at high temperatures. From the high-angle annular dark-field scanning TEM (HAADF-TEM) image and energy dispersive X-ray spectroscopy (EDS) elemental mappings of NFPP-U0.5% (Fig. 1h), it is evident that the locations of the S element correspond well with the sites of other elements in NFPP. Furthermore, the areas containing the carbon element indicate that the carbon coating is uniform. TEM images (Fig. S2) show that the sample, after S doping in the carbon layer, is composed of irregular nanoparticles with sizes below 100 nm. This is likely due to the formation of C–S bonds that stabilize the carbon structure, effectively inhibiting the expansion and agglomeration of NFPP particles during the sintering process. This greatly reduces the size of the grains. To further investigate the morphologies of the NFPP, NFPP-S and NFPP-U0.5%, we characterized the samples via Brunauer–Emmett–Teller (BET) and Raman spectra. BET was employed to evaluate the specific surface areas and porosity of all samples. As shown in Fig. 1i, the

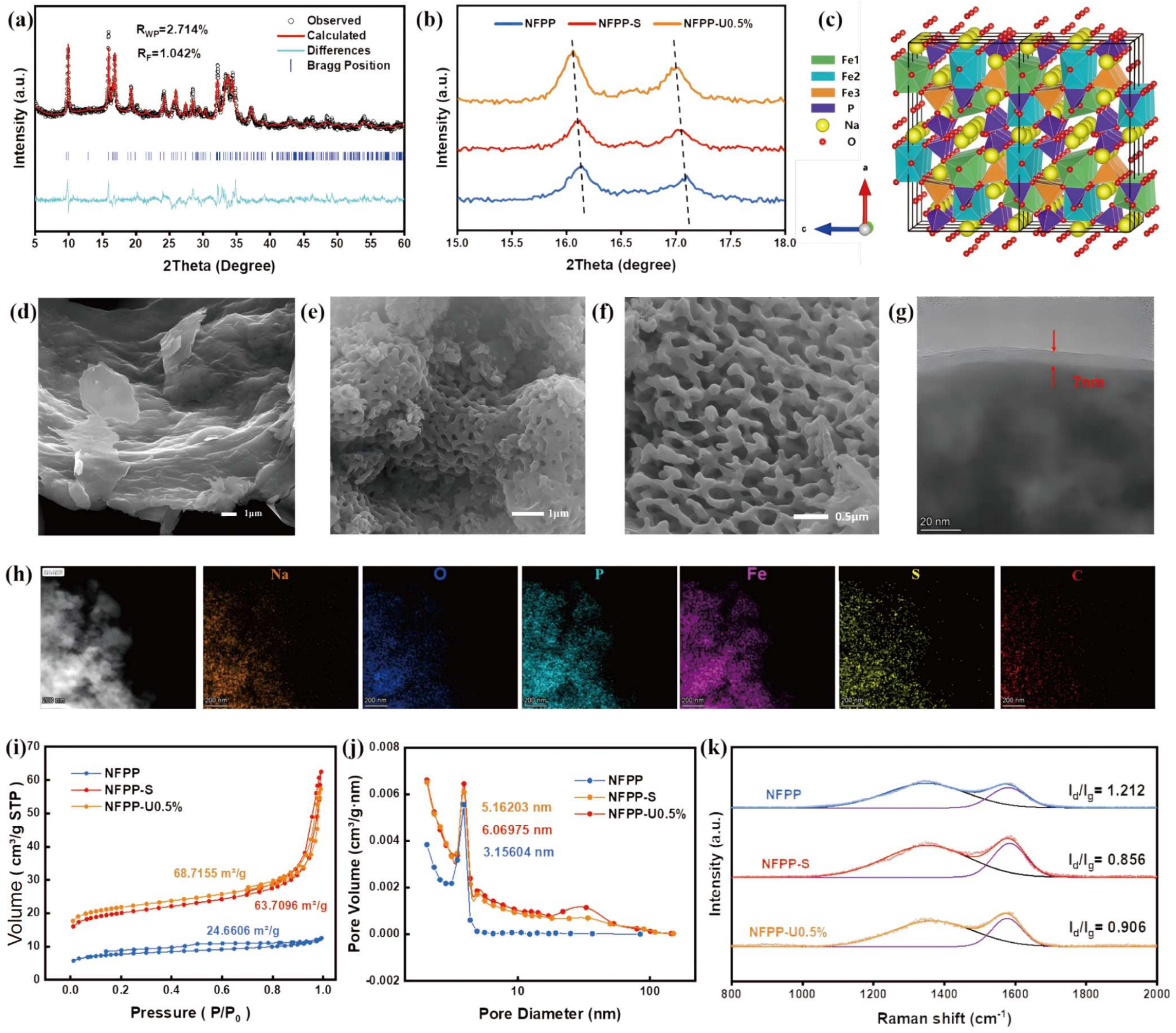

Figure 1 Materials characterizations. (a) Rietveld refinement of XRD pattern of NFPP-U0.5%. (b) XRD peak shift of NFPP, NFPP-S and NFPP-U0.5%. (c) Schematic for the crystal structure of NFPP. SEM images of (d) NFPP, (e) NFPP-S, and (f) NFPP-U0.5%. (g) TEM image of NFPP-U0.5%. (h) HAADF-TEM image and EDS elemental mappings of NFPP-U0.5%. (i) Surface area map. (j) Aperture profile of all samples. (k) Raman spectra of all samples.

isotherms of all three samples belonged to Type IV isotherms. This allows for the determination of pore size and distribution through analysis of the isotherm hysteresis loops. The specific surface area of NFPP-S (63.7069 $m^2\ g^{-1}$) and NFPP-U0.5% (68.7155 $m^2\ g^{-1}$) are much higher than that of NFPP (24.6606 $m^2\ g^{-1}$) which is consistent with SEM characterization. Besides, the adsorption average pore width of the BET test in Fig. 1j reveals that, compared to the NFPP-S and NFPP-U0.5%, NFPP does not have pores with diameters between 10 and 100 nm. These pores likely form due to the SO_2 produced by SO_4^{2-} decomposition at high temperature, along with the volatilization of S which comes from the SO_2 reduced at high temperature with C and H_2 [46,48]. The relatively larger surface area and abundant pore volume observed in NFPP-S and NFPP-U0.5% are attributed to the coral-like structure. This structure increases the contact area and provides more channels for electrolyte diffusion, offering abundant electrochemical active sites and improving sodium-ion diffusion.

Moreover, we also applied the Raman test to explore the structure of the carbon materials. In the Raman spectra of carbon materials, the D-peak represents the degree of defects in the carbon layer, while the G-peak corresponds to the tensile vibration of the C atom sp^2 mixed plane. Usually, we use the ratio of peak D to peak G (I_d/I_g) to analyze whether the carbon material tends to be amorphous or graphitized. We fitted the spectra and calculated the I_d/I_g of all samples. Results are shown in Fig. 1k. The I_d/I_g of NFPP, NFPP-S, and NFPP-U0.5% are 1.212, 0.856, and 0.906, respectively. The I_d/I_g of NFPP-S and NFPP-U0.5% are much lower than that of NFPP, indicating that the carbon layer containing S element possesses a higher graphitization degree. This is most likely due to the fact that S element will form the stable C–S–C bond in the carbon layer to improve the stability of the carbon layer [49]. Generally, a higher degree of graphitization in the carbon layer indicates greater stability, making the structure less likely to collapse during cycling. Consequently, the carbon layer structure of the S-containing samples will be more stable than that of the non-S-containing samples. Besides, we also found that the I_d/I_g of NFPP-U0.5% is a little higher than that of the NFPP-S. This is probably because the addition of S elements can produce certain defects on the carbon layer with the increase of S content. In addition to the C–S–C bonds, S doping in the carbon layer also exists in forms such as C=S. The presence of these S species introduces defects into the carbon lattice. As the overall S content increases, the concentration of these specific S configurations also rises, consequently leading to the defects in the carbon layer increase [50]. The existence of these defects is also conducive to the conduction of sodium ions [46].

To explore how the carbon coating affects the NFPP, XPS test was applied to all samples. In the high resolution Fe 2p spectra (Fig. 2a, d, g), two peaks located at around 710.8 and 724.5 eV are observed, which are identified as Fe $2p_{3/2}$ and Fe $2p_{1/2}$, respectively [42,51]. Compared to NFPP, a peak centered at 714 eV for samples which have S in the carbon layer (NFPP-S and NFPP-U0.5%) emerges, representing the interaction of C–S–Fe between the carbon layer and NFPP [47,52–58]. Additionally, Fe $2p_{3/2}$ and Fe $2p_{1/2}$ peaks of NFPP-S and NFPP-U0.5% have lower binding energy values than those of NFPP, which can be attributed to the electron transfer from Fe to more electronegative S due to the C–S–Fe interaction [47]. In Fig. 2c, f, i, the C 1s spectra are fitted. Peaks at binding energies of 286.15, 286.29 and 286.31 eV correspond to C–O for NFPP and C–O/C–S for NFPP-S and NFPP-U0.5%. The peaks around 287.72, 288.05 and 288.14 eV belong to the C=O bond, and the peaks at

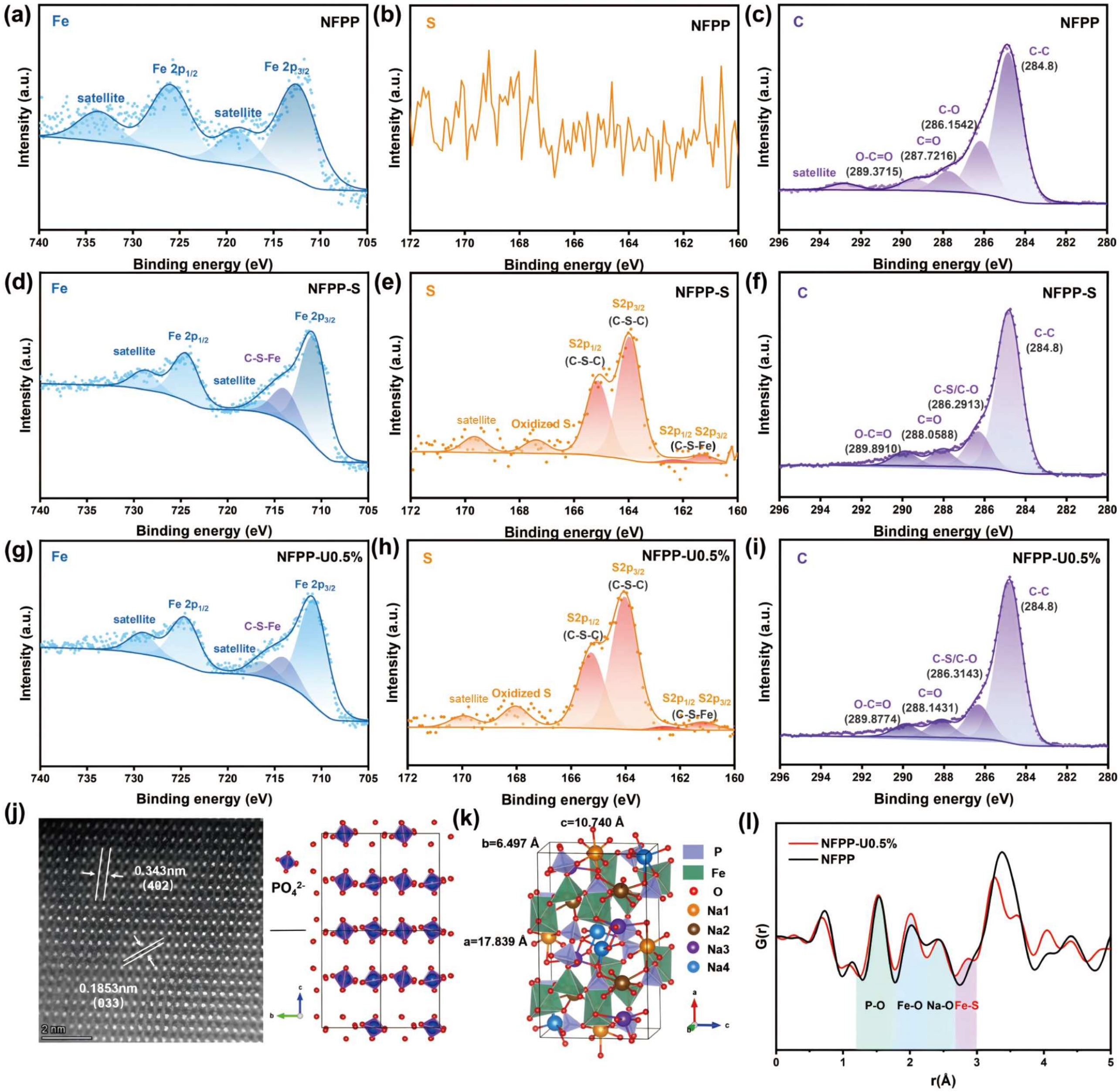

Figure 2 XPS spectra of NFPP (a) Fe 2p, (b) S 2p, (c) C 1s. XPS spectra of NFPP-S (d) Fe 2p, (e) S 2p, (f) C 1s. XPS spectra of NFPP-U0.5% (g) Fe 2p, (h) S 2p, (i) C 1s. (j) HAADF-STEM and the corresponding lattice of NFPP-U0.5%. (k) Lattice structure of NFPP-U0.5% constructed by XRD refinement and HAADF-STEM images. (l) PDF patterns of NFPP and NFPP-U0.5%.

around 289 eV correspond to O–C=O. In Fig. 2b, e, h, we analyzed the characteristic peaks of S. As the result shows, no characteristic peaks are found in NFPP, which does not contain S. However, in NFPP-S and NFPP-U0.5%, the 2p peak of S has spin-orbit splitting, and we can confirm that the characteristic peaks at 163.96, 164.02 and 165.12, 165.26 eV correspond to the S $2p_{1/2}$ and S $2p_{3/2}$ of C–S–C bond. The length of the C–S–C bond (0.178 nm) is longer than that of C–C bond (0.154 nm), the formation of C–S–C bond in carbon layers can increase the distance between layers which is favorable for transport of sodium ion [46]. Minor peaks at 161.28, 161.14 and 162.30, 162.53 eV are identified as the S $2p_{1/2}$ and S $2p_{3/2}$ of Fe–S. Considering the structure between the carbon layer and NFPP, along with the Fe 2p spectrum, we considered the peaks to be C–S–Fe [47,59]. Furthermore, the peak centered at around 168 eV should be ascribed to the sulfate species (–SO_x–) [60], owing to the unavoidable surface partial oxidation of carbon layer in the air. The presence of C–S–Fe strengthens the contact between the carbon layer and NFPP, making the carbon layer structure less likely to collapse during cycling. It also acts as a stabilizing chain for the crystal structure of NFPP, which will be further reflected in the electrochemical characterization of the material.

Furthermore, to investigate the reason for the increased S content, we analyzed the N 1s spectra of NFPP, NFPP-S, and NFPP-U0.5%. Besides, XPS tests were also conducted on NFPP-NON, NFPP-NON-U0.5%, and NFPP-NON-U1%. N 1s spectrum analysis on NFPP, NFPP-S, and NFPP-U0.5% is shown in Fig. S3. It was found that N elements in these materials mainly exist in four forms within the carbon layers: pyrrolic N, pyridinic N, graphitic N, and oxidized N. Among them, pyrrolic N and pyridinic N are active N sites. Pyrrolic N has a unique five-membered ring structure with a lone pair of electrons on the N atom, which makes it have a high chemical reactivity. Pyridinic N, located in a six-membered ring with sp^2 hybridized orbitals, has a lone pair of electrons that do not participate in conjugation. Although it is less active than pyrrolic N, its chemical reactivity is still high. By comparing the relative intensity ratios of XPS peaks, it was observed that samples containing S had a relatively higher content of pyrrolic N. Additionally, the intensity ratios of the peaks indicated that the addition of urea increased the signal of the oxidized N peak, suggesting an increase in its relative content. This is likely related to the increased S content, as S is unstable during the doping process and readily combines with oxygen to form SO_x by-products. This not only reduces the S content incorporated into the carbon layers but also significantly decreases the stability of the carbon materials. The introduction of N can effectively inhibit the combination of S and oxygen, potentially increasing the S content in the carbon layers. The XPS testing results of NFPP-NON, NFPP-NON-U0.5%, and NFPP-NON-U1% are shown in Fig. S4. The forms of N are more evident in the high-resolution N 1s spectra. It can be seen that NFPP-NON shows no signal for N, which is consistent with experiment design and verifies the accuracy of the CHONS test. In contrast, the N 1s spectra of N-containing materials NON-U0.5% and NFPP-NON-U1% show characteristic peaks for pyrrolic N, pyridinic N, and oxidized N, with the largest increase in pyrrolic N content, consistent with the N spectrum analysis results of the third chapter samples. The appearance of oxidized N in the N spectrum supports the hypothesis that the increase in S content is likely due to the reaction of active site N with oxygen to form oxidized N, thereby effectively inhibiting the combination of S and oxygen.

Moreover, we combined HAADF-STEM with XRD refinement to help construct the lattice structure of NFPP-U0.5%. As Fig. 2j shows, we obtained the clear atomic image. Comparing it with the NFPP lattice structure, we determined that the bright spot in the figure represents the PO_4^{2-} group. After matching the atomic image, the interplanar spacing of (402) (003) crystal faces was determined to be 0.343 and 0.1853 nm, respectively, matched well with the results calculated from refined lattice parameters. Therefore, we established a lattice model of NFPP-U0.5% based on the refined XRD data and HAADF-STEM which is shown in Fig. 2k. The Na^+ extraction sequence of NFPP is Na3 (5-coordinated) → Na1 (6-coordinated) → Na4 (6-coordinated). It is worth noting that the last Na^+ located at Na2 (7-coordinated) can not be extracted [61,62]. The X-ray pair distribution function (PDF), which is sensitive to the distance between atomic pairs, is also employed to study the atomic structure. After comparison with the NFPP-U0.5% model, we ensure that the distinct peaks at around 1.5, 2.0, and 2.4 Å correspond to the P–O, Fe–O, and Na–O atomic pairs, respectively (Fig. 2l). Compared to NFPP, a minor peak at around 2.85 Å appears. After comparing it with the NFPP-U0.5% model and reviewing the literature, we believe that this is the peak of Fe–S [59,63].

Electrochemical properties

Cyclic voltammetry (CV) of NFPP-U0.5% was carried out at a scan rate of 0.1 mV s^{-1}. As displayed in Fig. 3a, no obvious discrepancies are found over the three cycles, which indicates the good reversibility of NFPP-U0.5%. Two pairs of main redox peaks at 2.994/2.835 and 3.27/3.17 V along with a pair of weak peaks at 3.21/3.09 V are observed, suggesting a multi-step sodium-ion extraction/insertion process in NFPP-U0.5%. The oxidation peaks at 2.994/2.835 V correspond to the extraction of Na-ion at Na3 (5-coordinated) and Na1 (6-coordinated) sites. Additionally, the oxidation peaks at 3.20 and 3.28 V are attributed to the extraction of Na-ion at Na4 site (6-coordinated). Fig. 3b displays the galvanostatic charge/discharge profiles of three samples at 0.2 C (theoretical specific capacity = 129 mAh g^{-1}) within the voltage of 1.5–4.0 V. To exclude the effect of carbon material on performance, we subtract the mass of carbon coating in the capacity calculation. The C-rate performances of the three samples are displayed in Fig. 3c. The charge was conducted at the same current rate with the discharge process. The discharge capacities of NFPP-U0.5% are much higher than those of the NFPP at rates of 0.2, 0.5, 1, 2, 5, 10 C and even up to 20 C. It is worth noting that the performance of NFPP-S sample lags behind NFPP-U0.5% starting from 5 C. However, the discharge capacity of all three samples can almost fully recover when the rate returns to 0.1 C, reflecting the excellent endurance of NFPP at high C-rates.

Fig. 3d, e display the electrochemical cycling of NFPP, NFPP-S and NFPP-U0.5% at 0.2 and 1 C respectively. At the rate of 0.2 C, capacities of NFPP-S and NFPP-U0.5% remain stable over the 500 cycles, while NFPP shows significant capacity loss. At 1 C, NFPP-S and NFPP-U0.5% still exhibit impressive cycle stability, with 90.87% and 96.24% capacity retention after more than 1000 cycles, while the capacity retention of NFPP is only 49.49%. The fluctuation after 400 cycles in Fig. 3d was caused by the malfunction in the temperature-controlled battery test chamber. Furthermore, the long-term cycling stability of NFPP-

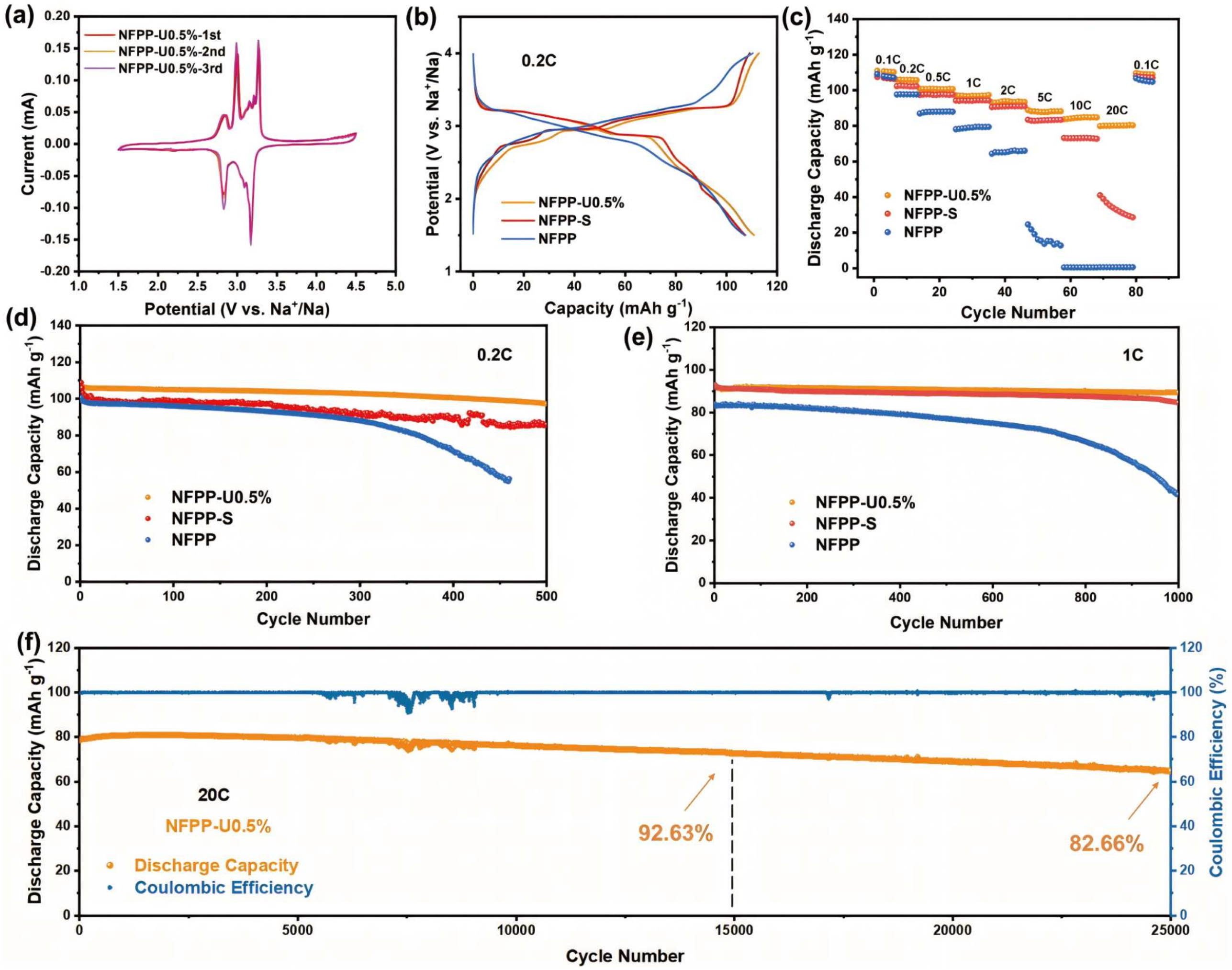

Figure 3 Electrochemical performance. (a) CV curves for the initial three cycles of NFPP-U0.5% at the scan rate of 0.1 mV s^{-1} and the voltage range of 1.5–4.0 V (vs. Na^+/ Na). (b) Charge/discharge profiles. (c) Rate performance of NFPP, NFPP-S and NFPP-U0.5%. (d) Cycling performance of NFPP, NFPP-S and NFPP-U0.5% at 0.2 C. (e) Cycling performance of NFPP, NFPP-S and NFPP-U0.5% at 1 C. (f) Long-term cycling performance of NFPP-U0.5% at 20 C.

U0.5% was evaluated at 20 C (Fig. 3f). After 15,000 cycles at 20 C, a capacity retention of 92.63% is still retained, and after 25,000 cycles, 82.66% still remained. The fluctuations between 5000 and 10,000 cycles were caused by drastic temperature changes due to a malfunction in the temperature-controlled battery chamber, but the battery subsequently returned to normal operation. It is significantly better than NFPP, which has a capacity retention of only 54.6% after 15,000 cycles (Fig. S6). Even among the NFPP-based cathode materials for SIBs reported so far, the performance of NFPP-U0.5% is also impressive (Table S3). Besides, in order to figure out if the N in the carbon layer would influence the cyclic stability of NFPP, cycling tests were conducted on NFPP-NON, NFPP-NON-U0.5% and NFPP-NON-U1%. As shown in Fig. S5, there is no significant difference in the cyclic stability of the three samples at 1 C, indicating that the N content in the raw materials has little/no impact on the cycling performance of the modified NFPP. The improvement in cycling performance is more likely related to the presence of S.

Dynamics

The rate performance is closely related to the sodium ion diffusion and the electron conductivity of the cathode materials. We first applied electrochemical impedance spectroscopy (EIS). The EIS plots (Fig. 4a) showed that NFPP-S and NFPP-U0.5% have smaller semicircle compared to NFPP, indicating that lower charge transfer resistance (R_{CT}) is achieved after S doping. To further compare the R_{CT} of three samples, EIS plots were fitted using an equivalent circuit model (insert of Fig. 4a). In the model, R_S stands for solution (electrolyte) resistance, R_C for contact resistance and R_{CT} for transfer resistance. The fitting results (Table S4) show that the R_{CT} of NFPP-S and NFPP-U0.5% are 89.34 and 76.17 Ω, which are lower than that of NFPP (317.3 Ω). The results indicate that moderate S doping can improve the electronic conductivity which is one of the most crucial factors for enhancing C-rate performance. Typically, carbon coating modifications improve conductivity via the outer carbon layer and do not alter the intrinsic electronic conductivity of the cathode material itself. However, the formation of C–S–Fe interactions affects the crystal structure of NFPP in the layers in contact with the carbon layer. To a certain extent, it also influences the electron energy-level distribution of NFPP, thereby causing a change in the band structure. The above prediction was validated through UV-vis to investigate the band

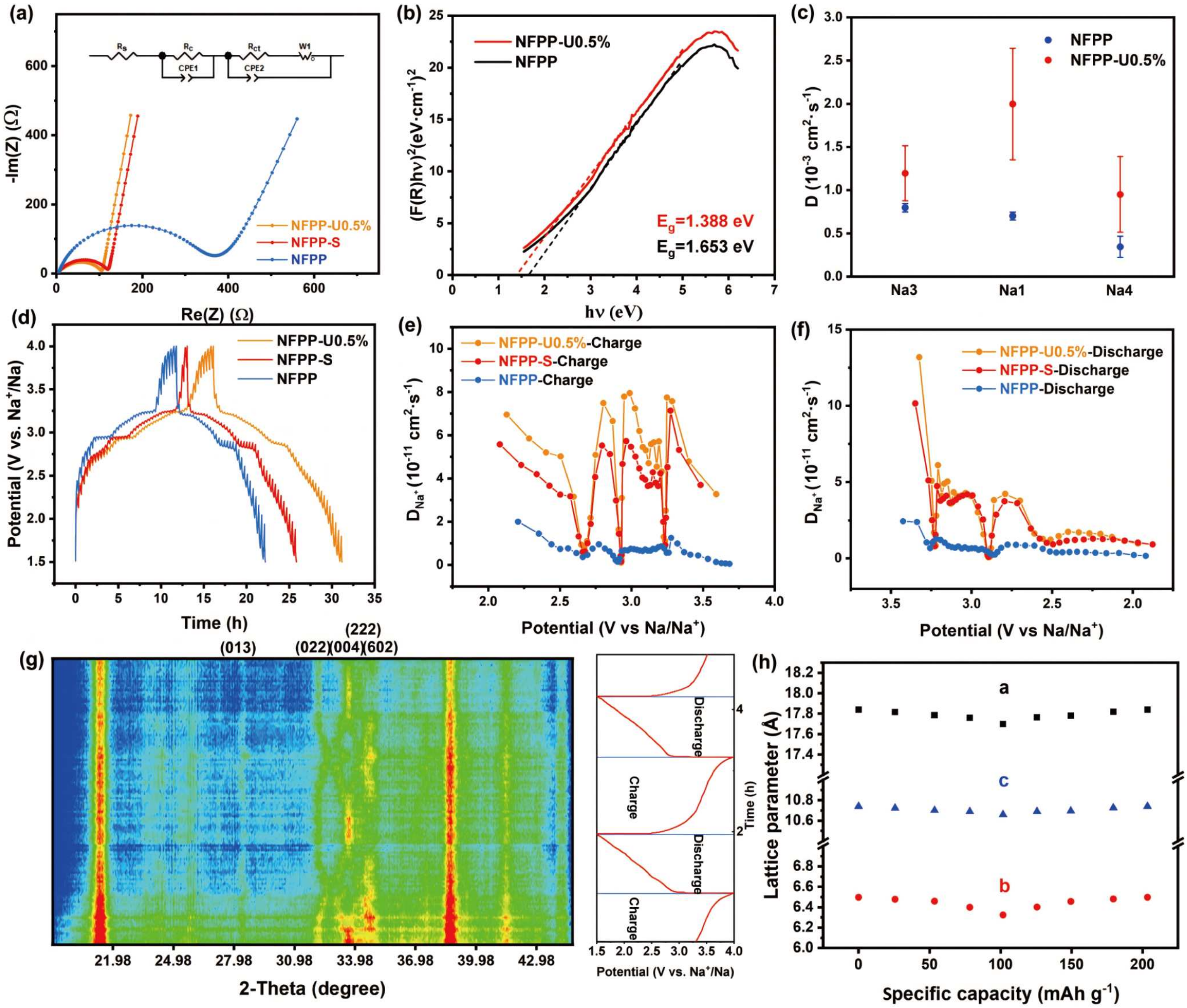

Figure 4 Na-ion dynamics. (a) EIS plots and equivalent circuit fitting results of NFPP, NFPP-S, and NFPP-U0.5% after 5 cycles at 1 C and the equivalent circuit model (inset). (b) UV-vis. (c) Diffusion coefficient calculated through AIMD. (d) GITT curves of NFPP-U0.5%. (e) Na-ion diffusivities of NFPP, NFPP-S, and NFPP-U0.5% during discharge process calculated from the GITT test. (f) Na-ion diffusivities of NFPP, NFPP-S, and NFPP-U0.5% during charge process calculated from the GITT test. (g) *In-situ* XRD patterns and corresponding potential-time plot of NFPP-U0.5%. (h) Changes in lattice parameters produced by the insertion/extraction of Na^+.

gaps and electron conductivity of NFPP and NFPP-U0.5%. As shown in Fig. 4b, we calculated the band gap with the Tauc-plot method. The optical band gaps of NFPP and NFPP-U0.5% were 1.653 and 1.388 eV, respectively [64]. The findings suggest that the S-doped carbon layer can reduce the band gap of NFPP which makes it easier for electrons to transition between energy bands, thereby reducing electronic transition resistance and improving the conductivity of the material.

In addition to electronic conductivity, the diffusion of sodium ions is also a key to the rate performance. The *ab initio* molecular dynamics (AIMD) simulations were carried out in NFPP and NFPP-U0.5% to obtain the diffusion coefficient D of Na3, Na1 and Na4. As shown in Fig. 4c, the Na^+ diffusion coefficient D of NFPP-U0.5% is higher on average than that of NFPP (the simulation process is shown in Fig. S8). To further verify the improvement of sodium ion diffusion by S doping, we applied the galvanostatic intermittent titration technique (GITT) to get the sodium-ion diffusivities. Based on the GITT test (Fig. 4d), the sodium-ion diffusivities were calculated (the detailed calculation method is displayed in Fig. S7). During the discharge and charge process (Fig. 4e, f), the calculated sodium-ion diffusivities of three samples exhibit a similar trend. In the potential range of main discharge plateaus (2.6–3.4 V vs. Na^+/Na) and main charge plateaus (2.1–3.6 V vs. Na^+/Na), the S-doped samples (NFPP-S and NFPP-U0.5%) display higher sodium-ion diffusivities than NFPP, demonstrating that the S doping enhances the sodium-ion diffusion in NFPP.

Furthermore, to validate the stabilizing role of the C–S–Fe during the cycle, we combined *in-situ* XRD and refinement for the analysis. The *in-situ* XRD patterns of NFPP-U0.5% and corresponding potential time profiles are displayed in Fig. 4g. The structural evolution is shown in Fig. S9. During the sodium-ion extraction process, the (022) and (222) diffraction peaks of NFPP-U0.5% shift to a higher angle, and reversibly return to initial states during the Na^+ insertion. Thus, it can be confirmed that the Na^+ insertion/extraction in NFPP-U0.5% is a one-phase structural evolution [36,48]. Fig. 4h shows the changes of lattice parameters during the cycle, which was calculated from *in-situ* XRD. The lattice shrinks during the extraction of Na^+, corresponding to a small volume change of approximately 4.1% during one cycle. The small volume change guarantees the long-term cycling stability. Combining the previous characterizations, the unique coral-like structure of the S-doped carbon layer enables the electrolyte to better infiltrate the electrode material. Additionally, this porous structure shortens the diffusion path of sodium ions into the cathode material. Consequently, the sodium-ion diffusion performance of NFPP-U0.5% is significantly enhanced. Moreover, the S in the carbon layer, while strengthening the stability of the carbon layer by forming C–S–C bonds, also forms C–S–Fe interactions with NFPP. This not only makes the carbon coating more stable but also greatly improves the cycling stability of NFPP. In addition, the C–S–Fe interactions affect the band gap of NFPP to a certain extent, increasing its electronic conductivity. The enhanced ionic and electronic conductivities endow NFPP-U0.5% with excellent rate performance.

CONCLUSIONS

We have successfully synthesized porous coral-like NFPP-U0.5% via a feasible and simple sol-gel method. The kinetic analysis results reveal that the S doping improves the Na-ion diffusivity and reduces the interfacial charge transfer resistance. Through XPS and PDF tests, we have identified the presence of the interaction of C–S–Fe. The unique coral-like porous carbon layer structure shortens the transport path of sodium ions into the cathode, and its high electrical conductivity also improves the conductivity of the composite cathode material. In addition, the presence of C–S–Fe interactions changes the structure of NFPP in contact with the carbon layer, thereby reducing the band gap of the cathode material and enhancing the intrinsic electronic conductivity of the material. The interaction of C–S–Fe enhances the stability between the cathode material and the carbon coating layer. The unique coral-like carbon structure together with the interaction of C–S–Fe enhanced the rate performance and enabled NFPP an ultra-long cycling life. NFPP-U0.5% achieved impressive rate performances (80.3 mAh g^{-1} at 20 C) and excellent cycling stability at room temperature (82.66% capacity retention after 25,000 cycles at 20 C). HAADF-STEM, *in-situ* XRD, AIMD, and GITT testing confirm the fast sodium diffusion, highly stable structure, and excellent electrochemical reversibility of NFPP-U0.5%. It is believed that the low cost, long-term cycling stability, and simple synthesis make NFPP-U0.5% a promising cathode material for SIBs. This work also provides valuable insights for the design and synthesis of low-cost, high-performance SIB cathodes.

Received 27 March 2025; accepted 25 June 2025;

1 Cao Y, Li M, Lu J, *et al.* Bridging the academic and industrial metrics for next-generation practical batteries. Nat Nanotechnol, 2019, 14: 200–207

2 Dong Y, Chen Y, Zeng Q, *et al.* Challenges and strategies of fast-charging Li-ion batteries with a focus on Li plating. Energy Mater Adv, 2024, 5: 0113

3 Yue J, Li S, Chen S, *et al.* Initiating high-voltage multielectron reactions in NASICON cathodes for aqueous zinc/sodium batteries. Energy Mater Adv, 2023, 4: 0050

4 Tufail MK, Zhai P, Jia M, *et al.* Design of solid electrolytes with fast ion transport: computation-driven and practical approaches. Energy Mater Adv, 2023, 4: 0015

5 Zhang J, Wang Y, Kang Y, *et al.* Cathode recycling of spent sodium ion batteries. Energy Mater Adv, 2024, 5: 0128

6 Fan D, Shen Q, Li H, *et al.* Redox couple modulation in NASICON phosphates toward high-performance cathodes for Na-ion batteries. Energy Mater Adv, 2024, 5: 0073

7 Gabriel E, Ma C, Graff K, *et al.* Heterostructure engineering in electrode materials for sodium-ion batteries: recent progress and perspectives. eScience, 2023, 3: 100139

8 Wang Z, Tang C, Wang Z, *et al.* High-energy $Na_4MnCr(PO_4)_3$@C cathode for solid-state sodium metal batteries. Energy Mater Adv, 2023, 4: 0036

9 Bai J, Li Z, Wang X, *et al.* Limitations and strategies toward high-performance red phosphorus materials for Li/Na-ion batteries. Energy Mater Adv, 2024, 5: 0086

10 Xu X, Guo L, Zhou J, *et al.* Efficient and composition-tolerant kesterite $Cu_2ZnSn(S,Se)_4$ solar cells derived from an *in situ* formed multifunctional carbon framework. Adv Energy Mater, 2021, 11: 2102298

11 Bera PK, Majumdar S, Ouillon G, *et al.* Quantitative earthquake-like statistical properties of the flow of soft materials below yield stress. Nat Commun, 2020, 11: 9

12 Fang Y, Zhao J, Su Y, *et al.* Understanding of spinel phases in lithium-rich cathode for high-energy-density lithium-ion batteries: a review. Energy Mater Adv, 2024, 5: 0115

13 Brant WR, Mogensen R, Colbin S, *et al.* Selective control of composition in prussian white for enhanced material properties. Chem Mater, 2019, 31: 7203–7211

14 Nai J, Lou XWD. Hollow structures based on prussian blue and its analogs for electrochemical energy storage and conversion. Adv Mater, 2019, 31: 1706825

15 Guo Z, Qian G, Wang C, *et al.* Progress in electrode materials for the industrialization of sodium-ion batteries. Prog Nat Sci-Mater Int, 2023, 33: 1–7

16 Wang C, Liu L, Zhao S, *et al.* Tuning local chemistry of P2 layered-oxide cathode for high energy and long cycles of sodium-ion battery. Nat Commun, 2021, 12: 2256

17 Xu L, Chen S, Su Y, *et al.* Building better batteries: solid-state batteries with Li-rich oxide cathodes. Energy Mater Adv, 2023, 4: 0045

18 Han MH, Gonzalo E, Singh G, *et al.* A comprehensive review of sodium layered oxides: powerful cathodes for Na-ion batteries. Energy Environ Sci, 2015, 8: 81–102

19 Zuo W, Liu X, Qiu J, *et al.* Engineering Na^+-layer spacings to stabilize Mn-based layered cathodes for sodium-ion batteries. Nat Commun, 2021, 12: 4903

20 Huang ZX, Gu ZY, Heng YL, *et al.* Advanced layered oxide cathodes for sodium/potassium-ion batteries: development, challenges and prospects. Chem Eng J, 2023, 452: 139438

21 Ge X, Li H, Li J, *et al.* High-entropy doping boosts ion/electronic transport of $Na_4Fe_3(PO_4)_2(P_2O_7)$/C cathode for superior performance sodium-ion batteries. Small, 2023, 19: e2302609

22 Shi X, Hao Z, Zhu W, *et al.* $Na_4Fe_3(PO_4)_2(P_2O_7)$/C composite with porous structure enabling all-climate and long-life sodium-ion batteries. Sci China Mater, 2024, 67: 3622–3628

23 Xin S, Zhang X, Wang L, *et al.* Roadmap for rechargeable batteries: present and beyond. Sci China Chem, 2024, 67: 13–42

24 Kong LY, Liu HX, Zhu YF, *et al.* Layered oxide cathodes for sodium-ion batteries: microstructure design, local chemistry and structural unit. Sci China Chem, 2024, 67: 191–213

25 Liu YF, Hu HY, Li JY, *et al.* An air-stable single-crystal layered oxide cathode based on multifunctional structural modulation for high-energy-density sodium-ion batteries. Sci China Chem, 2024, 67: 4242–4250

26 Zou T, Gong Y, Li X, *et al.* Medium bandgap A-DA'D-A type small molecule acceptors prepared by synergetic modification strategy for efficient indoor organic photovoltaic devices. Sci China Mater, 2025, 68: 830–837

27 Shen W, Li H, Guo Z, *et al.* Improvement on the high-rate performance

of Mn-doped $Na_3V_2(PO_4)_3/C$ as a cathode material for sodium ion batteries. RSC Adv, 2016, 6: 71581–71588

28 Jungers T, Mahmoud A, Malherbe C, *et al.* Sodium iron sulfate alluaudite solid solution for Na-ion batteries: moving towards stoichiometric $Na_2Fe_2(SO_4)_3$. J Mater Chem A, 2019, 7: 8226–8233

29 Zhang H, Tan X, Li H, *et al.* Assessment and progress of polyanionic cathodes in aqueous sodium batteries. Energy Environ Sci, 2021, 14: 5788–5800

30 Tediashvili D, Gečė G, Pilipavičius J, *et al.* Synthesis, characterization, and degradation study of Mn-based phosphate frameworks ($Na_3MnTi(PO_4)_3$, $Na_3MnPO_4CO_3$, $Na_4Mn_3(PO_4)_2P_2O_7$) as aqueous Na-ion battery positive electrodes. Electrochim Acta, 2022, 417: 140294

31 Jin T, Li H, Zhu K, *et al.* Polyanion-type cathode materials for sodium-ion batteries. Chem Soc Rev, 2020, 49: 2342–2377

32 Fernández-Ropero AJ, Zarrabeitia M, Reynaud M, *et al.* Toward safe and sustainable batteries: $Na_4Fe_3(PO_4)_2P_2O_7$ as a low-cost cathode for rechargeable aqueous Na-ion batteries. J Phys Chem C, 2018, 122: 133–142

33 Li X, Zhang J, Zhang Y, *et al.* A facile ball-milling preparation strategy of nitrogen-doped carbon coated $Na_4Fe_3(PO_4)_2P_2O_7$ nano-flakes with superior sodium ion storage performance. Chem Eng Sci, 2022, 260: 117951

34 Belotserkovsky VA, Kosova NV, Gainutdinov II. Modeling of chemical and electrochemical Na^+/Li^+ ion exchange in cathode material $Na_4Fe_3(PO_4)_2P_2O_7$. Mater Today-Proc, 2020, 25: 501–504

35 Wang L, Wang J, Wang L, *et al.* Synergistic strain suppressing and interface engineering in $Na_4MnV(PO_4)_3/C$ for wide-temperature and long-calendar-life sodium-ion storage. ACS Nano, 2024, 18: 10863–10873

36 Boyadzhieva TJ, Koleva VG, Kukeva RR, *et al.* Mechanochemically desodiated $Na_4Fe_3(PO_4)_2P_2O_7$ as a lithium and sodium storage material. ACS Appl Energy Mater, 2021, 4: 7182–7189

37 Li X, Zhang Y, Zhang B, *et al.* Mn-doped $Na_4Fe_3(PO_4)_2(P_2O_7)$ facilitating Na^+ migration at low temperature as a high performance cathode material of sodium ion batteries. J Power Sources, 2022, 521: 230922

38 Chen Y, Fan Q, Li J, *et al.* Preparation and electrochemical performance of nanowire-shaped $Na_3Mn_{2-x}Fe_x(P_2O_7)(PO_4)$ for sodium-ion and lithium-ion batteries. Dalton Trans, 2022, 51: 4173–4181

39 Xiong F, Li J, Zuo C, *et al.* Mg-doped $Na_4Fe_3(PO_4)_2(P_2O_7)/C$ composite with enhanced intercalation pseudocapacitance for ultra-stable and high-rate sodium-ion storage. Adv Funct Mater, 2022, 33: 2211257

40 Qi X, Dong Q, Dong H, *et al.* Copper-induced lattice distortion in $Na_4Fe_3(PO_4)_2(P_2O_7)$ cathode enabling high power density Na-ion batteries with good cycling stability. Energy Storage Mater, 2024, 73: 103861

41 Qi X, Dong H, Yan H, *et al.* Hollow core-shelled $Na_4Fe_{2.4}Ni_{0.6}(PO_4)_2P_2O_7$ with tiny-void space capable fast-charge and low-temperature sodium storage. Angew Chem Int Ed, 2024, 63: e202410590

42 Wang L, Wang L, Wang H, *et al.* Progress and perspective of high-entropy strategy applied in layered transition metal oxide cathode materials for high-energy and long cycle life sodium-ion batteries. Adv Funct Mater, 2025, 35: 2417258

43 Li Z, Li F, Xu X, *et al.* A scalable approach to $Na_4Fe_3(PO_4)_2P_2O_7$@carbon/expanded graphite as cathode for ultralong-lifespan and low-temperature sodium-ion batteries. Chin Chem Lett, 2025, 36: 110390

44 Harizanova S, Tushev T, Koleva V, *et al.* Carbon-based composites with mixed phosphate-pyrophosphates with improved electrochemical performance at elevated temperature. Materials, 2023, 16: 6546

45 Yuan T, Wang Y, Zhang J, *et al.* 3D graphene decorated $Na_4Fe_3(PO_4)_2(P_2O_7)$ microspheres as low-cost and high-performance cathode materials for sodium-ion batteries. Nano Energy, 2019, 56: 160–168

46 Zhou T, Chen Y. Thiourea induced the N/S co-doped carbon skeleton suppressing the dissolution of V to boost superior cyclic stability of $Na_3V_2(PO_4)_3$. Carbon, 2024, 218: 118778

47 Zhu J, Wei P, Zeng Q, *et al.* MnS@N,S Co-doped carbon core/shell nanocubes: sulfur-bridged bonds enhanced Na-storage properties revealed by *in situ* Raman spectroscopy and transmission electron microscopy. Small, 2020, 16: e2003001

48 Li W, Zhou M, Li H, *et al.* A high performance sulfur-doped disordered carbon anode for sodium ion batteries. Energy Environ Sci, 2015, 8: 2916–2921

49 Li Y, Chen M, Liu B, *et al.* Heteroatom doping: an effective way to boost sodium ion storage. Adv Energy Mater, 2020, 10: 2000927

50 Grigonis A, Medvid A, Onufrijevs P, *et al.* Graphitization of amorphous diamond-like carbon films by laser irradiation. Optical Mater, 2008, 30: 749–752

51 Zhao A, Yuan T, Li P, *et al.* A novel Fe-defect induced pure-phase $Na_4Fe_{2.91}(PO_4)_2P_2O_7$ cathode material with high capacity and ultra-long lifetime for low-cost sodium-ion batteries. Nano Energy, 2022, 91: 106680

52 Chen W, Zhang X, Mi L, *et al.* High-performance flexible freestanding anode with hierarchical 3D carbon-networks/Fe_7S_8/graphene for applicable sodium-ion batteries. Adv Mater, 2019, 31: 1806664

53 Zhang H, Liu B, Lu Z, *et al.* Sulfur-bridged bonds heightened Na-storage properties in MnS nanocubes encapsulated by S-doped carbon matrix synthesized via solvent-free tactics for high-performance hybrid sodium ion capacitors. Small, 2023, 19: e2207214

54 Chen Y, Li S, Chen J, *et al.* Sulfur-bridged bonds enabled structure modulation and space confinement of MnS for superior sodium-ion capacitors. J Colloid Interface Sci, 2024, 664: 360–370

55 Paredes Camacho RA, Wu AM, Jin XZ, *et al.* Effective carbon constraint of MnS nanoparticles as high-performance anode of lithium-ion batteries. J Power Sources, 2019, 437: 226931

56 Gao X, Wang B, Zhang Y, *et al.* Graphene-scroll-sheathed α-MnS coaxial nanocables embedded in N, S Co-doped graphene foam as 3D hierarchically ordered electrodes for enhanced lithium storage. Energy Storage Mater, 2019, 16: 46–55

57 Wang F, Liu Z, Feng H, *et al.* Engineering C–S–Fe bond confinement effect to stabilize metallic-phase sulfide for high power density sodium-ion batteries. Small, 2023, 19: e2302200

58 Aboelazm E, Seong Khe C, Grätz S, *et al.* Layered construction of integrated sulfur-bridged CoNi-S/rGO architecture for enhanced electrochemical energy storage. Chem Eng J, 2024, 490: 151557

59 Yan D, Xiao S, Li X, *et al.* NiS_2/FeS heterostructured nanoflowers for high-performance sodium storage. Energy Mater Adv, 2023, 4: 0012

60 Xu D, Chen C, Xie J, *et al.* A hierarchical N/S-codoped carbon anode fabricated facilely from cellulose/polyaniline microspheres for high-performance sodium-ion batteries. Adv Energy Mater, 2016, 6: 1501929

61 Gao J, Tian Y, Mei Y, *et al.* Robust NASICON-type iron-based $Na_4Fe_3(PO_4)_2(P_2O_7)$ cathode for high temperature sodium-ion batteries. Chem Eng J, 2023, 458: 141385

62 Chen M, Hua W, Xiao J, *et al.* NASICON-type air-stable and all-climate cathode for sodium-ion batteries with low cost and high-power density. Nat Commun, 2019, 10: 1480

63 Zhu M, Northrup P, Shi C, *et al.* Structure of sulfate adsorption complexes on ferrihydrite. Environ Sci Technol Lett, 2013, 1: 97–101

64 Xi Y, Wang X, Wang H, *et al.* Optimizing the electron spin states of $Na_4Fe_3(PO_4)_2P_2O_7$ cathodes via Mn/F dual-doping for enhanced sodium storage. Adv Funct Mater, 2023, 34: 2309701

Acknowledgement This work was supported by the National Natural Science Foundation of China (52272234), the National Key Research and Development Program of China (2020YFA0715000), the International Science and Technology Cooperation Program of Hubei Province (2024EHA039), and the Independent Innovation Project of Hubei Longzhong Laboratory (2022ZZ-20).

Author contributions Xu L and Dou Z provided theoretical guidance for this research. Cai Y designed and engineered the samples; Cheng H and Chen Z performed some experiments; Cai Y wrote the paper with support from Xu H. All authors contributed to the general discussion.

Conflict of interest The authors declare that they have no conflict of interest.

Supplementary information Supplementary materials are available in the online version of the paper.

Yuyang Cai is a postgraduate student at Wuhan University of Technology (WUT) under the supervision of Prof. Lin Xu. His research interests include sodium-ion batteries and 3D-printing.

Hanwen Cheng got his Bachelor's degree in WUT. His research centers on the lithium-ion battery electrolyte and DFT simulation.

Zhuo Chen is a PhD student at WUT under the supervision of Prof. Liang Zhou. His research interests include electrode materials for electrochemical energy storage devices such as sodium-ion batteries.

Hantao Xu is a PhD candidate enrolled in 2021 in a joint program between WUT and the National University of Singapore. His research focuses on the application of electrolytes and electrode materials in secondary batteries.

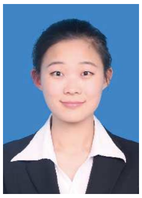

Zhenzhen Dou received her PhD degree from the School of Bioengineering, Dalian University of Technology. She is currently a postdoctoral researcher at WUT. Her research focuses on the development of colloidal particles and their applications in micro-energy storage devices.

Lin Xu is a professor at WUT. He received his PhD degree from the School of Materials Science and Engineering, WUT in 2013. He was a visiting graduate student from 2011 to 2013 and a postdoctoral researcher from 2013 to 2016 at Harvard University. His research focuses on nanomaterials and devices for energy storage and conversion.

高倍率及长循环稳定钠离子电池的硫掺杂碳界面相互作用促进$Na_4Fe_3(PO_4)_2(P_2O_7)$的动力学研究

蔡雨洋[1,2†], 程翰文[2†], 陈卓[2†], 徐翰涛[2†], 李士栋[1,2], 李景昊[2], 张艺博[1,2], 赵历[2], 豆珍珍[2*], 徐林[1,2,3,4*]

摘要 铁基混合磷酸盐因其低成本、无毒性及高结构稳定性，被视为钠离子电池(SIBs)极具潜力的正极材料．然而，其电子电导率低下和离子扩散缓慢严重制约了电化学性能．本研究提出一种具有多孔珊瑚状硫掺杂碳层的$Na_4Fe_3(PO_4)_2(P_2O_7)$（NFPP)作为SIBs正极材料．硫掺杂碳层的多孔珊瑚状结构与C–S–Fe界面相互作用显著改善了电子电导率和钠离子扩散动力学．NFPP-U0.5%展现出优异的倍率性能，在20 C高倍率下仍可保持约80.3 mAh g^{-1}的可逆容量．原位X射线衍射分析进一步证实，独特的C–S–Fe界面结合特殊碳结构设计，使材料在循环过程中晶格体积变化率显著降低．经25,000次20 C高倍率循环后，容量保持率达82.66%，展现出超长循环寿命．该硫掺杂碳包覆NFPP正极材料凭借卓越的电化学性能与独特的界面相互作用，为低成本、长寿命储能系统提供了极具潜力的解决方案．